Molecularly Bridged Design of Electron-Delocalized Dual Redox-Active Organic Electrode for High-Efficiency Capacitive Deionization and Water Treatment

Xinyue Zhang[a], Haoyuan Qiu[a], Zhiyong Han[a], Lei Ke[c], Mugilan Narayanasamy[d], Can Cui[a], Jun Yang[a*], Minjie Shi[a], Edison Huixiang Ang[b,*]

[a]*School of Materials Science and Engineering, Jiangsu University of Science and Technology, Jiangsu 212003, P. R. China*

[b]*Natural Sciences and Science Education, National Institute of Education, Nanyang Technological University, Singapore 637616, Singapore*

[c] *Jiangsu Hilong Technology Co. Ltd., Zhenjiang, 212003, P. R. China*

[d]*Department of Chemical Sciences and Bernal Institute, University of Limerick, Castletroy, V94 T9PX, Limerick, Ireland*

* *Corresponding authors.*

E-mail addresses: iamjyang@just.edu.cn (J. Yang); edison.ang@nie.edu.sg (E. H. Ang)

Experimental section

Material preparation

The synthetic protocol was initiated using commercially available starting materials, specifically perylene-3,4,9,10-tetracarboxylic dianhydride (PTCDA) and phenazine-2,3-diyldiamine (DAP), along with catalytic amounts of zinc acetate and imidazole as reaction mediators. All chemical precursors were employed as received without further purification steps. In a typical synthesis, stoichiometric quantities of PTCDA (0.8 mmol) and DAP (1.6 mmol) were combined with imidazole (117.6 mmol) and zinc acetate (0.23 mmol) in a rigorously dried glass ampoule under an inert atmosphere. The sealed ampoule was then subjected to thermal treatment at 160 °C for 24 h. After the thermal reaction, the system was allowed to cool to ambient temperature. The resulting product mixture was purified by filtration and successive washings with deionized water and tetrahydrofuran, followed by vacuum drying at 80 °C overnight to obtain the PTAP powder, with a yield ranging between 60-70%.

Structural characterizations

The morphology and microstructure of the synthesized PTAP molecule were evaluated by several characterization techniques, including scanning electron microscope (SEM; FEI Nova NanoSem450), nuclear magnetic resonance spectra (NMR; Bruker Avance III spectrometer, 400 MHz), Flourier transform infrared spectrometer (FT-IR; Thermo Fisher Scientific Nicolet 6700), X-ray photoelectron spectroscopy (XPS; KAlpha Thermo electron), X-ray diffraction (XRD; Bruker D8 X-ray spectrometer) equipped with a 2D detector (Cu Kα, λ=1.54 Å), and ultraviolet-visible spectrophotometer (UV-vis; UV-8000). Thermal gravimetric analysis (TGA; TGA5500) was carried out within an inert atmosphere at 10 °C min^{-1}.

Theoretical calculation

All calculations were performed by using the DFT method implemented in the commercial Gaussian 16 program package.[1] Gaussian 16 is a registered trademark of Gaussian, Inc. The structures of PTAP and its monomers were optimized at the B3LYP/def2-SVP level of theory. This combination of method, functional, and software was used to derive both the optimized molecular structures and the corresponding vibrational wave numbers for the compounds under investigation. In addition, the geometric configurations of the PTAP were optimized to achieve the lowest total energies. Localized orbital locator-π (LOL-π), reduced density gradient (RDG), Harmonic Oscillator Model of Aromaticity (HOMA), and molecular electrostatic potential (MESP) wave function cubes were achieved according to the Multiwfn 3.8 (dev) code, and were visually demonstrated by using the VMD software.[2] The ESP was obtained by solving the Poisson equation for the charge distribution and mapping it onto the molecular surface. The color-coded ESP maps indicate electron density distribution, where red represents electron-rich regions (negative ESP) and blue represents electron-deficient regions (positive ESP). The transition of molecular structures from PTAP to PTAP + $4Na^+$ and PTAP + $8Na^+$ follows a sequential reduction process. The energy changes were calculated using the Gibbs free energy change (ΔG) for each step. The reaction potential was given by: $E = -\Delta G/nF$, where n is the number of transferred electrons and F is the Faraday constant.

Electrochemical measurements

The PTAP electrode was prepared by combining the active material (PTAP), conductive agent (acetylene black), and binding agent (polyvinylidene fluoride) in a mass ratio of 7:2:1 (7 mg: 2 mg: 1 mg) within an N-methylpyrrolidone (NMP) solvent and continuously stirred to obtain a homogeneous mixture. This mixture was then uniformly coated onto graphite paper and dried under vacuum at 60 °C overnight. The electrochemical properties of the PTAP electrode were performed in 0.5 M NaCl aqueous electrolyte using an electrochemical workstation (DH7000C Donghua). In the testing configuration, the as-prepared PTAP electrode served as the working electrode, a graphite rod was used as the counter electrode and a saturated Ag/AgCl electrode was employed for reference electrode.

The contribution ratios from CV curves at different scan rates (2~50 mV s^{-1}) were quantified using Trasatti analysis (Eq. S1):

$$i = k_1 v + k_2 v^{1/2} \tag{S1}$$

where k_1 and k_2 were obtained by linearly fitting $i(V)/v^{1/2}$ vs $v^{1/2}$. As a result, $k_1 v$ and $k_2 v^{1/2}$ present the capacitive- and diffusion-controlled contribution, respectively.

GCD tests were measured at different current densities (1~8 A g^{-1}). The specific capacitance (C, F g^{-1}) calculated from the GCD curves was determined using the following Eq. S2:

$$C = \frac{I\Delta t}{m\Delta V} \tag{S2}$$

where I (A), Δt (s), ΔV (V) and m (g) correspond to discharge current, discharge time, potential window and active mass of the PTAP electrode, respectively.

EIS tests were implemented within the frequency range of 100 kHz to 0.01 Hz. The Na^+ diffusion process in the PTAP electrode was qualitatively calculated by diffusion coefficient (D, cm^2 s^{-1}) according to Eq. S3 and S4:

$$Z' = R_s + R_{ct} + \sigma\omega^{-1/2} \tag{S3}$$

$$D = \frac{R^2T^2}{2A^2n^4F^4C^2\sigma^2} \tag{S4}$$

where Z' and σ are the real part impedance and Warburg factor from the EIS plot, respectively. R, T, A, n, F and C refer to gas constant (8.314 J K^{-1} mol^{-1}), absolute temperature (298 K), electrode surface area (cm^2), number of transferred electrons, faraday constant and Na^+ concentration, respectively.

Desalination experiments

Desalination performance was evaluated using a hybrid CDI device, with the PTAP molecule acting as the anode and commercial activated carbon (AC) as the cathode. In order to inhibit the adsorption of anions during the reversal of voltage, an anion exchange membrane (AEM) was placed adjacent to the AC cathode. The assembly consisted of plexiglass plates (6 × 6 cm^2), 0.3 mm thick rubber spacers, and current collectors coated with active materials (4 × 4 cm^2), with a total electrode mass of 60 mg. A 40 mL NaCl solution (500 mg L^{-1}) was circulated at 10 mL min^{-1} using a peristaltic pump. Solution conductivity was continuously measured with a DDSJ-308F conductivity meter, with salt concentrations determined from a pre-calibrated conductivity-concentration curve. The desalination tests were conducted at voltages of 0.8, 1.0, 1.2, and 1.4 V for 30 min each, followed by a desorption step at the reverse voltage for an equivalent duration. The brackish water in this experiment was synthesized by adding NaCl to deionized water, resulting in an initial salinity of 500 mg L^{-1} and a conductivity of 1015 μS cm^{-1}. The CDI system consisted of three linked units for treating brackish water. Each unit operated at a fixed voltage of 1.2 V, with an adsorption time of 30 minutes per stage and a flow rate of 10 mL min^{-1}. Additionally, the system's ability to remove cationic dyes was tested using methylene blue (MB) as a representative pollutant. The initial MB concentration was set at 100 mg L^{-1}. The CDI process involved a 30-minute adsorption phase, with the dye solution circulating at 10 mL min^{-1} under a 1.2 V applied voltage. The removal efficiency was determined via UV-visible spectroscopy, where changes in absorption intensity over time indicated the remaining dye concentration in the effluent.

The desalination performances of the constructed CDI device were evaluated by salt removal capacity (SAC, mg g^{-1}), average salt removal rate ($ASAR$, mg g^{-1} min^{-1}), charge efficiency (Λ) and energy consumption (E, Wh g^{-1}) according to the following

Eq. S5-S8:

$$SAC = \frac{(C_0 - C_e) \times V}{m} \tag{S5}$$

$$ASAR = \frac{SAC}{t} \tag{S6}$$

$$\Lambda = \frac{m \times SAC \times F}{M \times \int Idt} \times 100\% \tag{S7}$$

$$E = \frac{U \times \int Idt}{3.6 \times (C_e - C_0) \times V} \tag{S8}$$

where C_0 and C_e (mg L^{-1}) are concentrations of influent and effluent saline water, respectively. V (L), m (g) and t (s) refer to the volume of saline solution, total mass of two electrodes and adsorption time, respectively. F (96485 C mol^{-1}), M (58.5 g mol^{-1}), I (A) and U (V) correspond to Faraday constant, molar mass of NaCl, transient current at the adsorption time and applied voltage, respectively. The CDI performance in cationic dye removal was evaluated using methylene blue (MB) as model contaminant, at a concentration of 100 mg L^{-1}. Dye concentrations were monitored via UV-vis spectrophotometry to quantify removal efficiency.

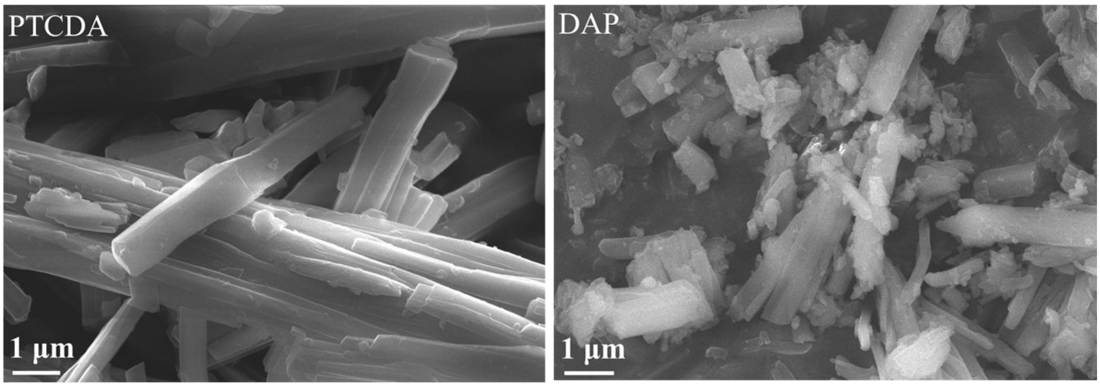

Fig. S1. SEM micrographs of PTCDA and DAP.

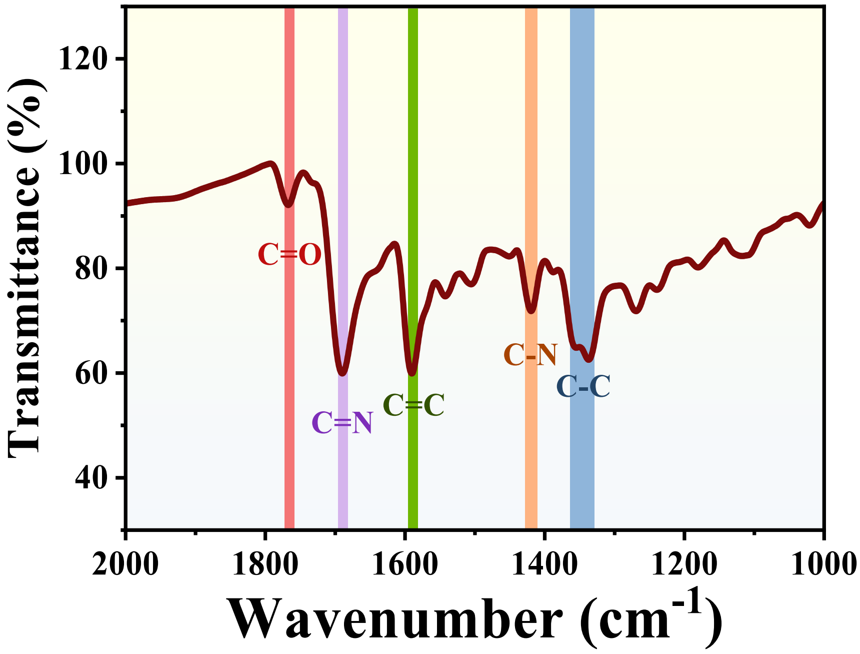

Fig. S2. FT-IR spectrum of the PTAP molecule.

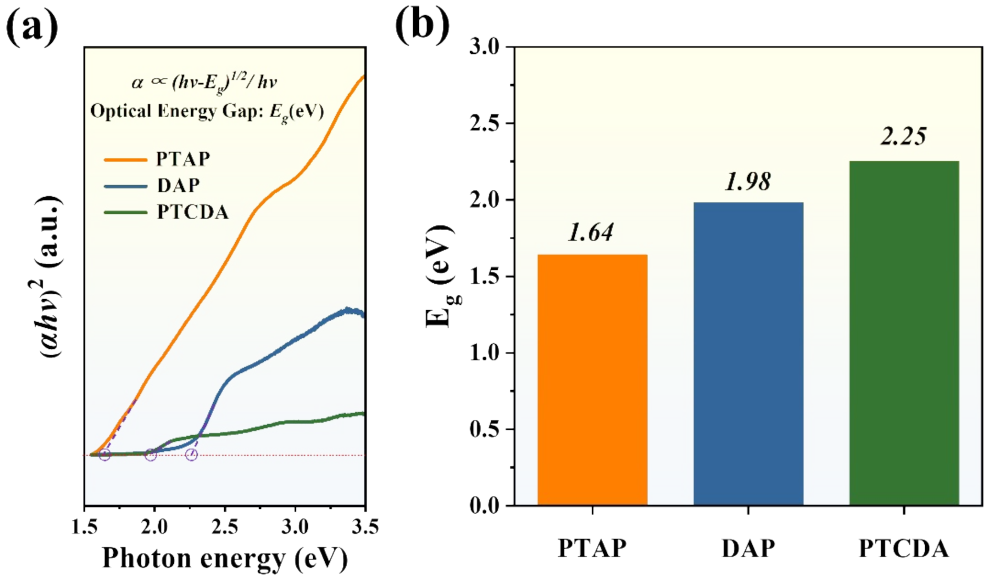

Fig. S3. (a) UV-Vis absorption spectra and (b) the calculated E_g values of PTCDA and DAP precursors as well as PTAP product.

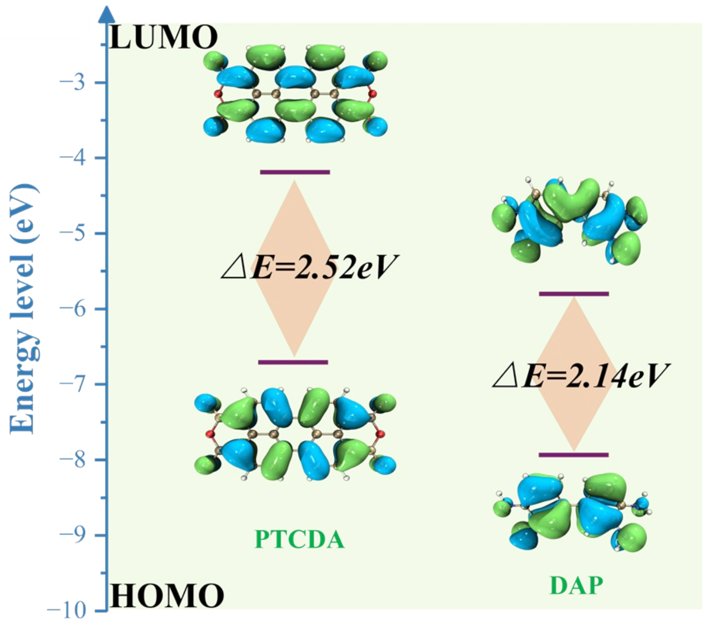

Fig. S4. HOMO/LUMO energy gaps of PTCDA and DAP.

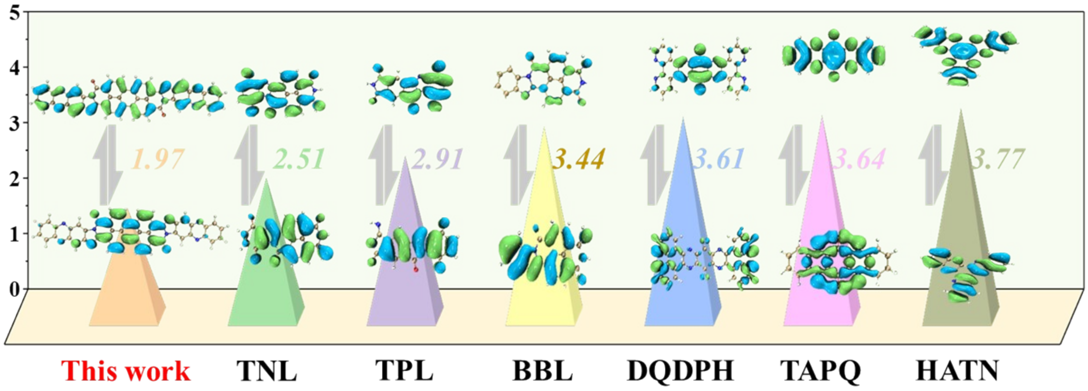

Fig. S5. The comparison of HOMO/LUMO gaps between the PTAP molecule and typical electroactive organic materials.

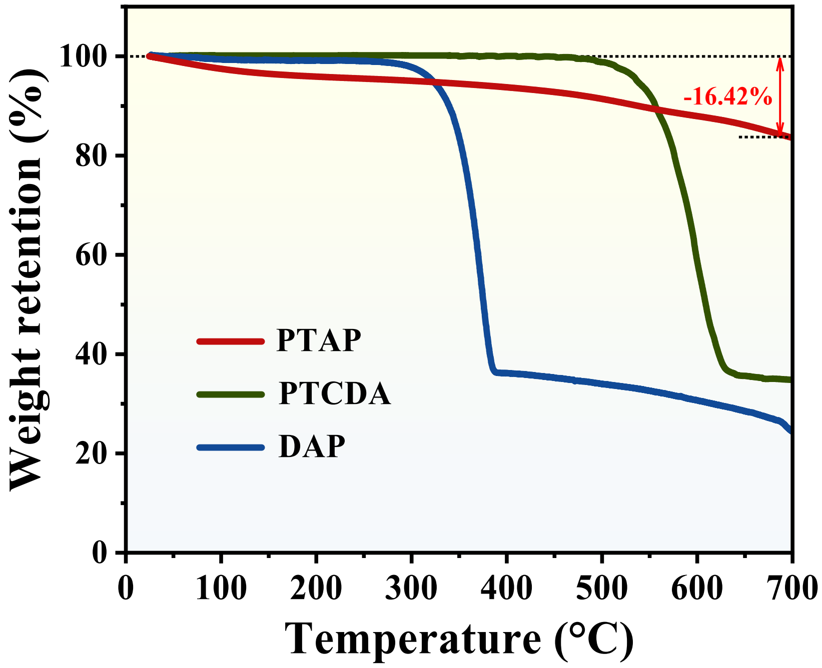

Fig. S6. TGA curves of PTCDA and DAP precursors as well as PTAP product.

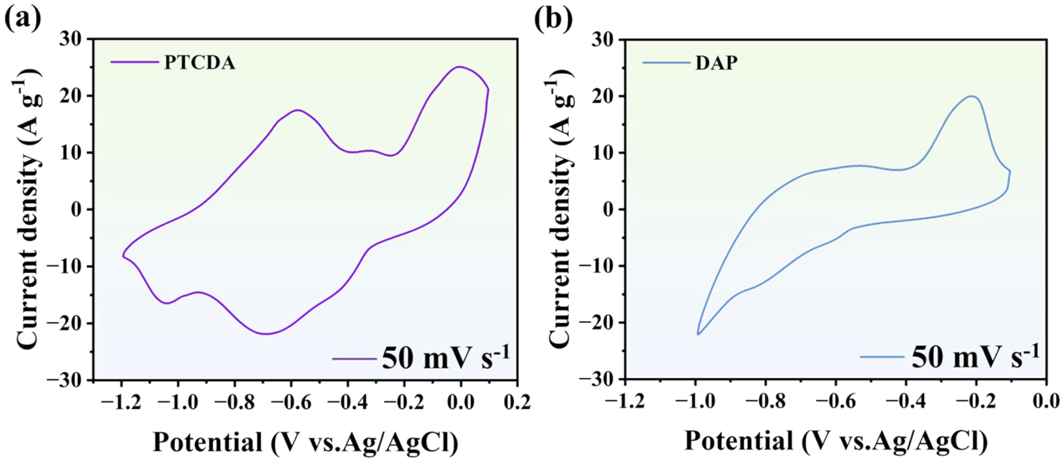

Fig. S7. The CV curves of (a) PTCDA and (b) DAP electrodes.

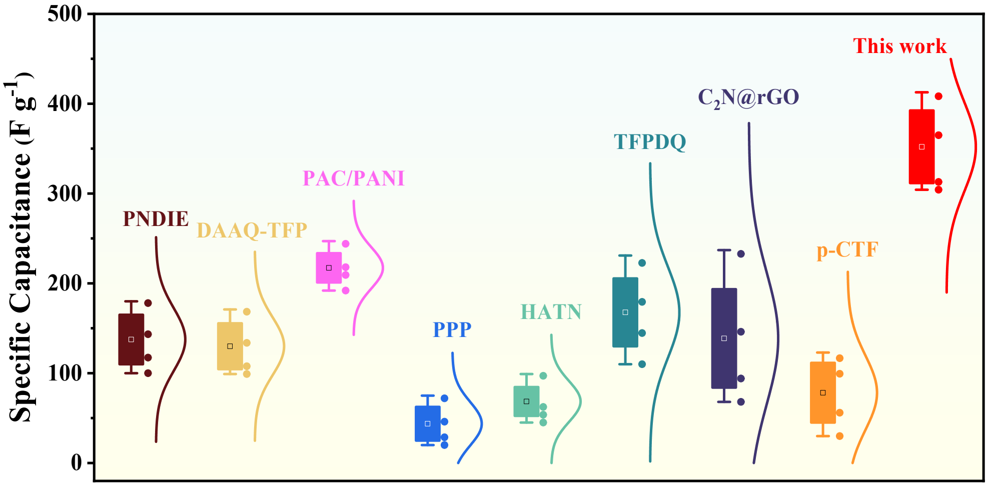

Fig. S8. Comparison of specific capacitances with reported organic electrodes for Na^+ capture.[3-10]

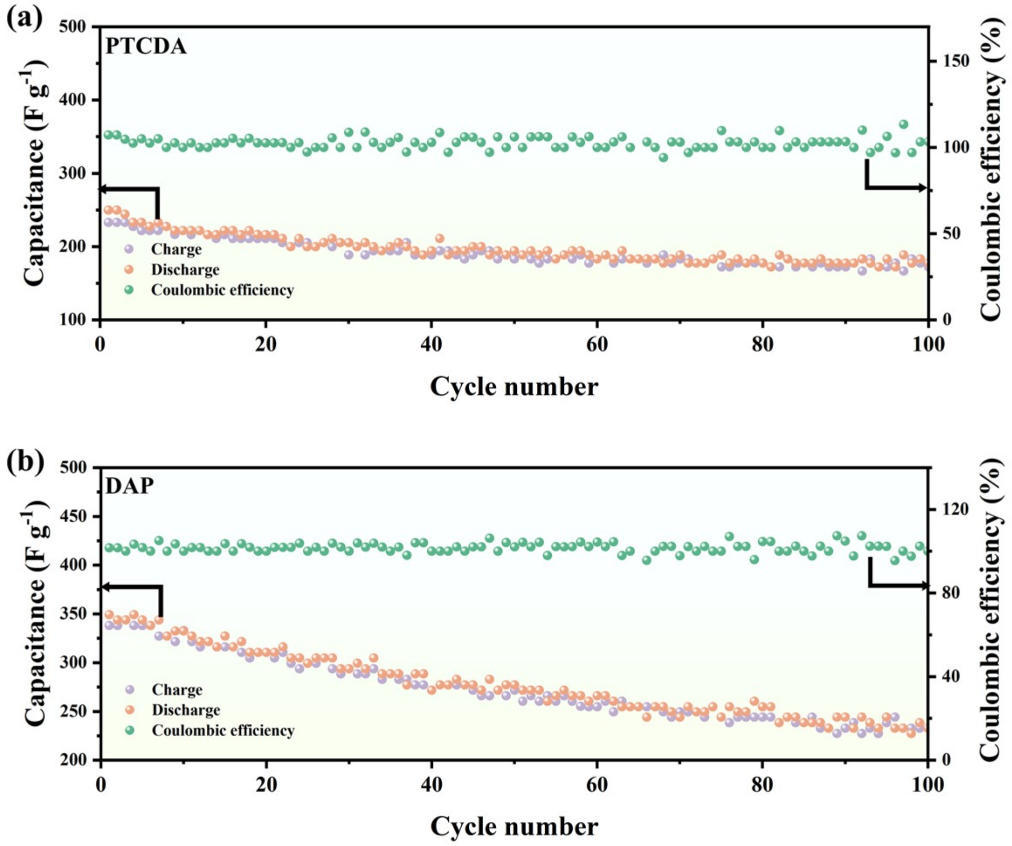

Fig. S9. Cycling performances of (a) PTCDA and (b) DAP electrodes at 1 A g^{-1}.

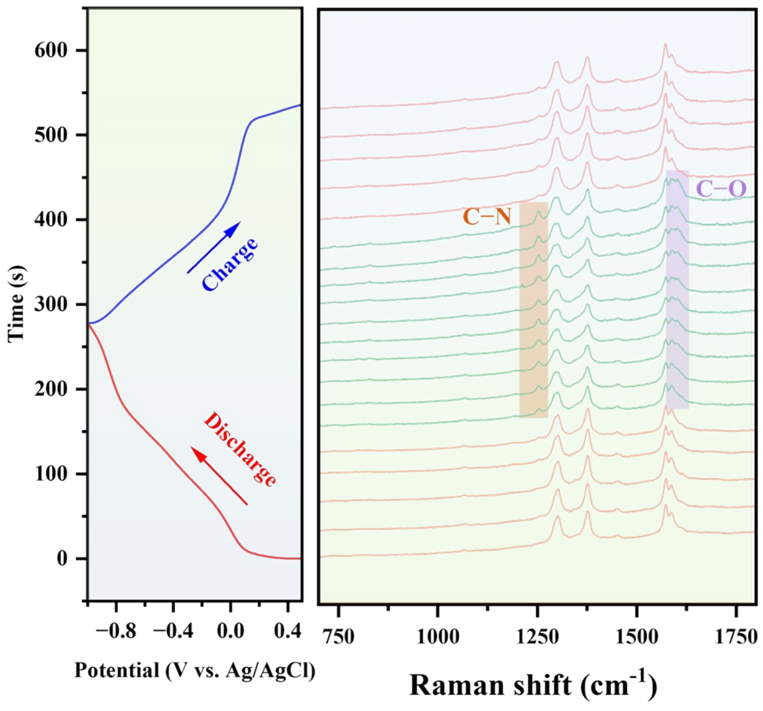

Fig. S10. In situ Raman spectroscopy of PTAP during electrochemical process.

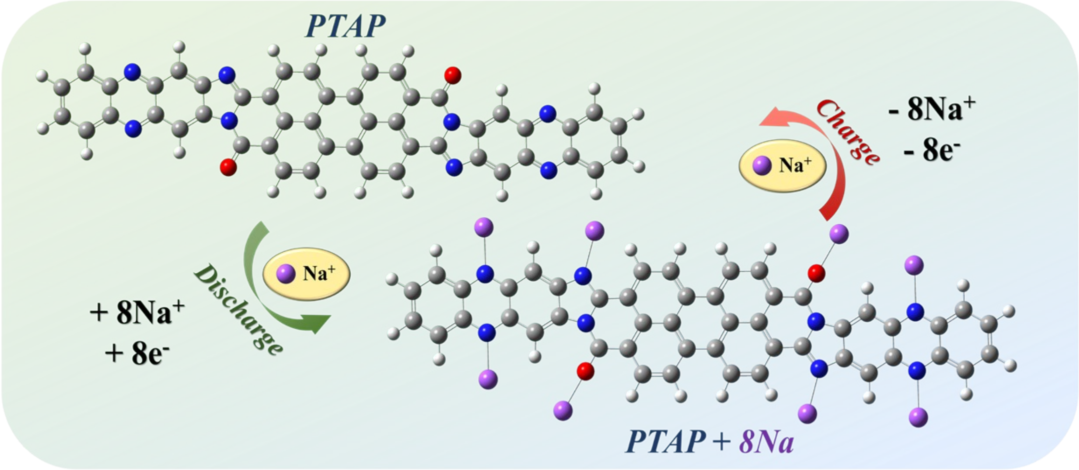

Fig. S11. Schematic illustration of the proposed Na^+ adsorption-desorption process within the PTAP electrode.

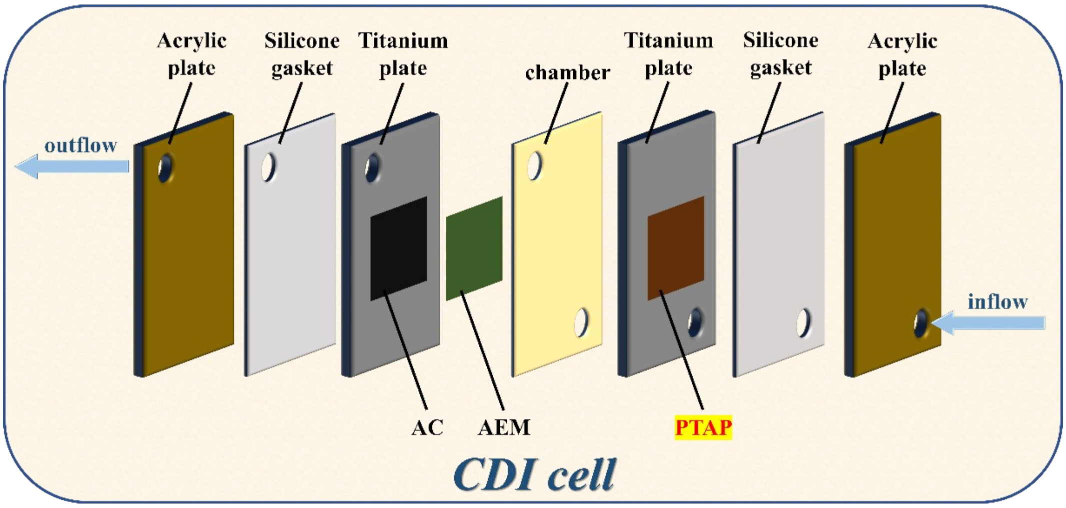

Fig. S12. Schematic diagram of the assembled CDI device.

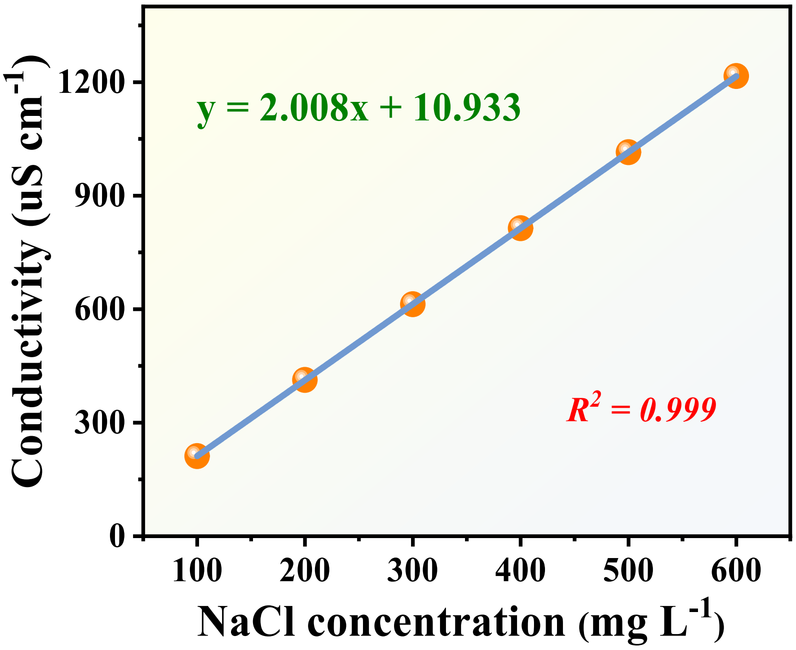

Fig. S13. The relationship between NaCl concentration and conductivity.

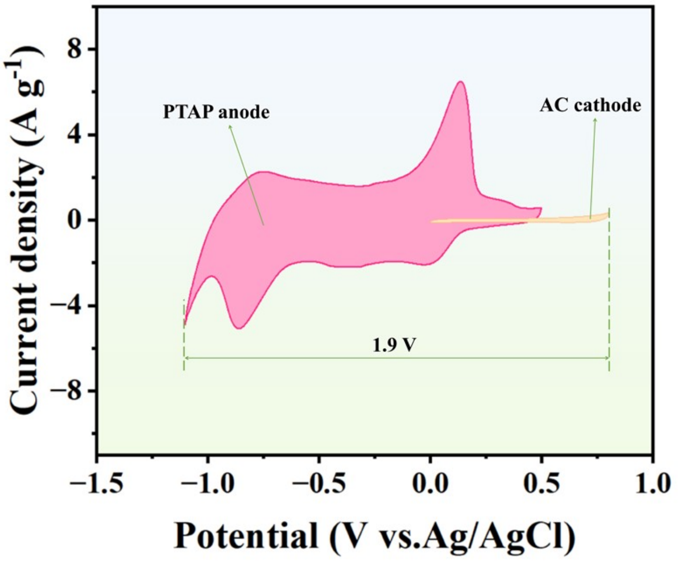

Fig. S14. CV curves of PTAP anode and AC cathode derived from three-electrode analysis within negative and positive potential ranges.

The electrochemical stability windows of the PTAP anode and AC cathode were assessed using three-electrode CV measurements (vs. Ag/AgCl) at 5 mV s^{-1} (Fig. S14). The CV results indicate that the PTAP anode demonstrates stable redox activity between –1.1 and 0.5 V, whereas the AC cathode shows capacitive behavior in the range of 0 to 0.8 V. This complementary potential distribution allows our asymmetric CDI device to operate safely over an extended voltage window of 0~1.9 V. Notably, this design overcomes the 1.23 V limitation typical of conventional symmetric CDI systems with identical electrodes, where the uniform potential distribution induces water splitting at lower applied voltages.

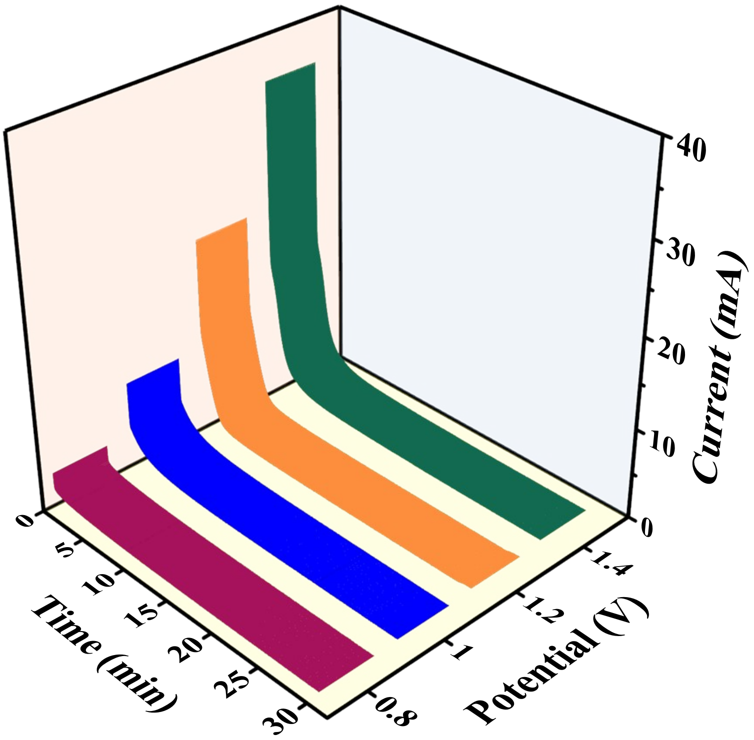

Fig. S15. Current response curves of the CDI device at various imposed voltages.

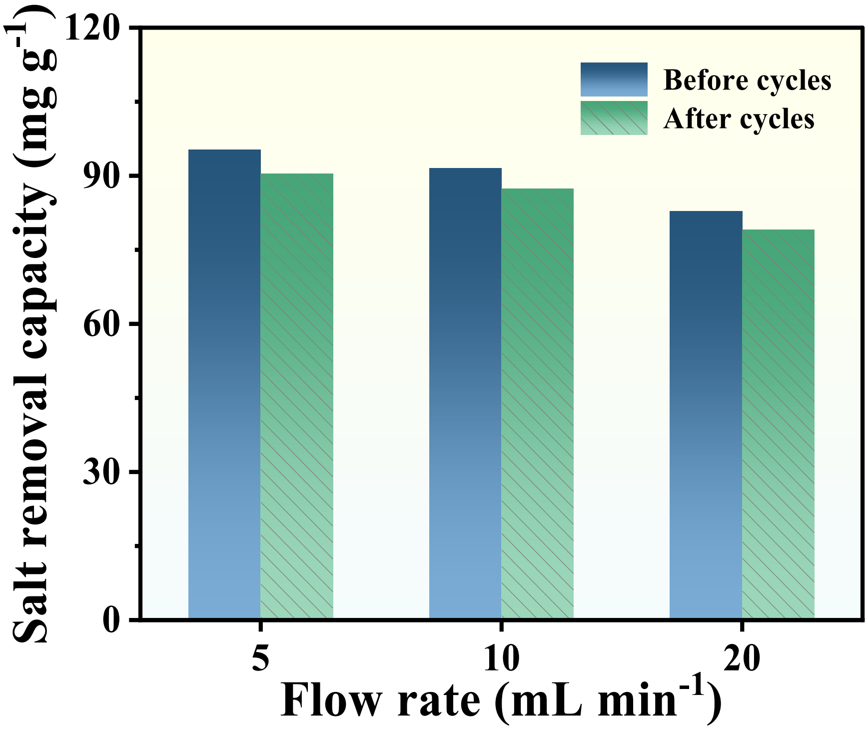

Fig. S16. Salt removal capacities of the CDI device at different inlet flow rates before and after cycles.

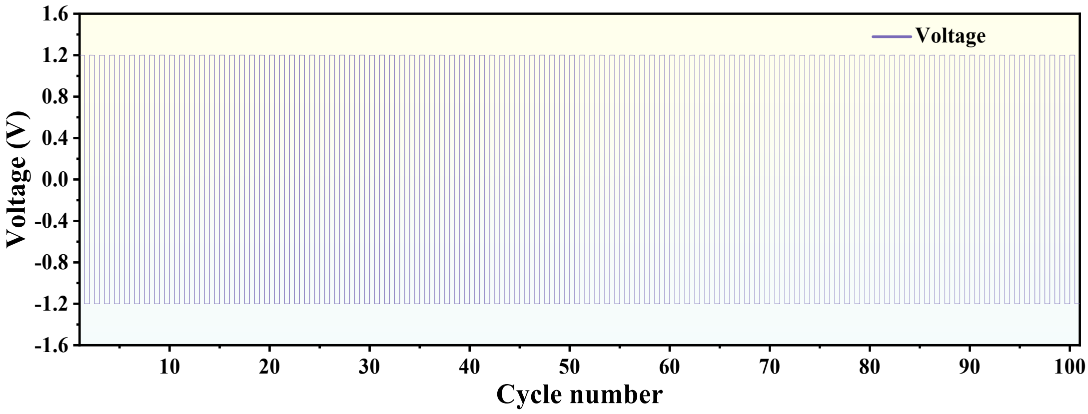

Fig. S17. The voltage values over repeated adsorption-desorption cycles.

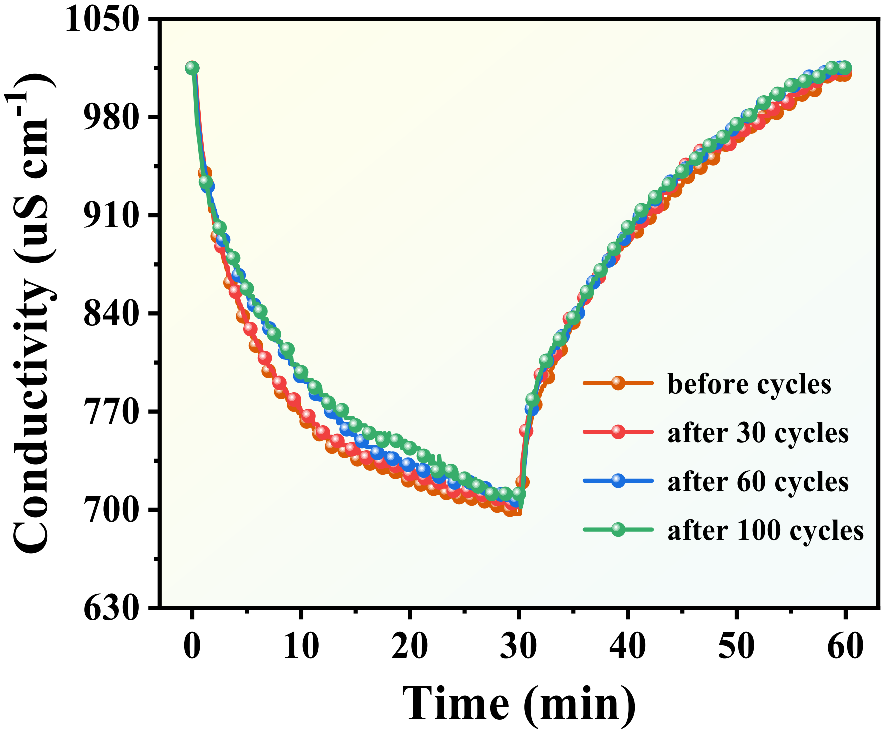

Fig. S18. Variation in solution conductivity throughout CDI treatment across different cycle numbers.

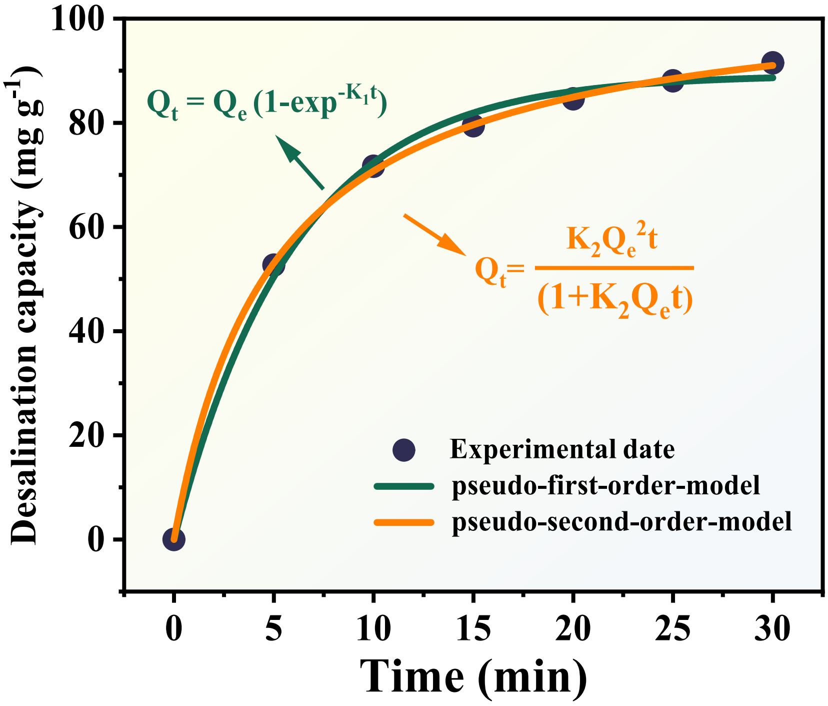

Fig. S19. Pseudo-first-order and pseudo-second-order kinetic models for Na^+ removal by the assembled PTAP-based CDI device at different times.

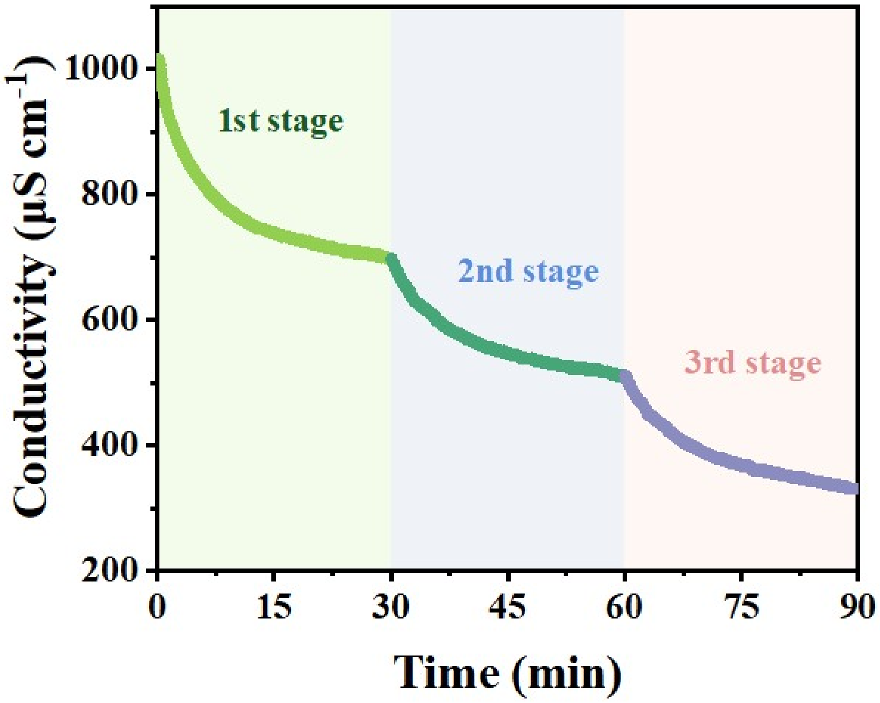

Fig. S20. Solution conductivity change at different stage.

Table S1. The obtained equivalent series resistance (R_s), charge transfer resistance (R_{ct}) and Warburg impedance (Z_w) of the PTAP electrode during the discharge/charge process from equivalent circuit fitting of EIS results.

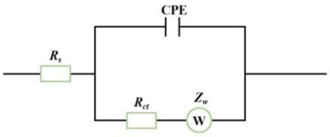	R_s (Ω)	R_{ct} (Ω)	Z_W (Ω)
Initial	**0.76**	**0.75**	**0.30**
Charge -0.7 V	**0.76**	**0.19**	**0.29**
Charge 0.1 V	**0.76**	**1.01**	**0.30**
Charge 0.5 V	**0.82**	**0.46**	**0.18**
Discharge -0.4 V	**0.84**	**0.21**	**0.16**
Discharge -0.9 V	**0.77**	**0.61**	**0.24**
Discharge -1.1 V	**0.73**	**1.18**	**0.34**

Electrochemical impedance spectroscopy (EIS) provides a comprehensive understanding of the kinetic properties within the PNDS electrode throughout the electrosorption process. Fig. 3a presents ex situ EIS profiles of the PTAP electrode at specific charged and discharged states, wherein the equivalent circuit diagram and corresponding fundamental parameters from the EIS data are listed in Table S2. All the Nyquist plots exhibit similar characteristics with nearly vertical straight lines in the low-frequency region, indicating a proficient Na^+ diffusion in the aqueous NaCl solution. It is worth noting that all of the interfacial charge-transfer resistance (R_{ct}) values are all <1.5 Ω, as indicated by the semicircle in the highfrequency region. This observation confirms the stability of the electrolyte/electrode interface and the rapid charge transfer process during the discharge/charge cycle.

Table S2. Performance metrics of CDI devices at different applied voltages.

Voltage (V)	**Salt removal capacity (mg g^{-1})**	**Average salt removal rate (mg g^{-1} min^{-1})**	**Peak salt removal rate (mg g^{-1} min^{-1})**	**Energy consumption (Wh g^{-1})**	**Charge efficiency (%)**
0.8	48.33	1.61	13.3	0.71	64.23
1.0	63.01	2.10	14.7	0.78	72.67
1.2	91.50	3.05	18.83	0.84	81.18
1.4	104.44	3.48	20.1	1.15	69.53

Table S3. Comparison of the salt removal performance of CDI devices using different organic electrodes with those reported previously (Fig. 5g).

Sample	**Salt removal capacity (mg g^{-1})**	**Salt removal rate (mg g^{-1} min^{-1})**
PAC/PANI	35.3	1.18
SiW12@PANI/EGC	29.34	0.58
HATN/MXene	57.5	1.92
PPy/CNT	43.99	0.53
mPDA/MXene	37.72	1.27
TFPDQGO	58.4	1.95
MXene@DAAQ-TFP-COF	53.1	1.77
PNDIE	54.2	1.81
Poly-p-phenylene	52.5	0.88
DAAQ-TFP-COF	22.8	0.76
This work	91.49541	3.04985

Table S4. The corresponding pseudo-first-order and pseudo-second-order kinetic parameters resulting from Fig. S19.

Sample	Pseudo-first-order		Pseudo-second-order	
PTAP	**Q_e (mg g^{-1})**	89.24	**Q_e (mg g^{-1})**	106.22
	K_1	0.16654	**K_2**	0.00188
	R^2	0.9958	**R^2**	0.9997

In order to investigate the important role of the PTAP electrode in the CDI system for Na^+ adsorption during the desalination process, the kinetic models were established based on the experimental data about the variation of Na^+ adsorption with desalination time. The rate-determining step is firstly described through the time-dominated pseudo-first-order and pseudo-second-order kinetic analysis. It is acknowledged that the pseudo-first-order pattern is typically used to depict the physical adsorption processes, whereas the pseudo-second-order pattern is commonly employed to characterize the chemical adsorption phenomena. As shown in Fig. S19, the adsorption kinetics of Na^+ within the PTAP electrode can be fitted preferably by the pseudo-second-order manner owing to its greater correlation coefficient (R^2=0.9958) compared to the pseudo-first-order manner (R^2=0.9997), suggesting that the chemical adsorption driven by the electric field is the primary determinant of Na^+ adsorption rate of the PTAP electrode, rather than slow diffusion-limited processes such as external diffusion and ion permeation. Remarkably, a substantial rate constant of 1.88×10^{-3} g mg^{-1} min^{-1} can be achieved, corroborating the rapid Na^+ adsorption kinetics of the PTAP electrode in the CDI device.

Table S5. Comparisons of salt removal capacity and average removal rate with other previously reported CDI devices under same imposed voltages.

	CDI devices	**Voltage**	**Salt removal capacity (mg g^{-1})**	**Average removal rate (mg g^{-1} min^{-1})**	**Ref.**
MXene-based materials	$Ti_3C_2T_x$//AC	1.2 V	20.27	1.01	11
	NiHCF@MXene//AC	1.2 V	30	1	12
	TiO_2@TiS_2//AC	1.2 V	36.45	0.52	13
	Fe_3O_4@$Ti_3C_2T_x$//AC	1.2 V	44	1.47	14
Metallic oxides or hydroxides	α-MnO_2//AC	1.2 V	19.64	0.33	15
	MnO_2//AC	1.2 V	21.32	0.36	16
	RGO@Mn_3O_4//AC	1.2 V	34.2	0.57	17
	Nb_2O_5@N-C//AC	1.2 V	35.4	0.3	18
	$ZnCo_2O_4$//AC	1.2 V	39.4	0.66	19
	ZnCo-Cl LDH//AC	1.2 V	56.1	0.94	20
	$CoMn_2O_4$//AC	1.2 V	60.7	1.01	21
	CuAl-LDO@rGO//AC	1.2 V	64	1.07	22
Metallic sulfides or selenides	MoS_2//AC	1.2 V	16.8	0.93	23
	VS_2@GP//AC	1.2 V	31.9	0.8	24
	MoS_2/CoS_2@TiO_2 //AC	1.2 V	44.22	0.74	25
	$MoSe_2$@MCHS//AC	1.2 V	45.25	1.51	26
	SnS_2@NC//AC	1.2 V	49.86	1.66	27
	PTAP//AC	**1.2 V**	**91.50**	**3.05**	**This work**

Reference

1. M. Frisch, G. Trucks, H. Schlegel, G. Scuseria, M. Robb, J. Cheeseman, G. Scalmani, V. Barone, G. Petersson and H. Nakatsuii, Gaussian 16, Revision A. 03, Gaussian, Inc., Wallingford CT. 3, 2016.
2. W. Humphrey, A. Dalke and K. Schulten, *J. Mol. Graph.*, 1996, **14**, 33-38.
3. D. Liu, X. Ning, Y. Hong, Y. Li, Q. Bian and J. Zhang, *Electrochim. Acta*, 2019, **296**, 327-334.
4. B. Li, Q. Cao, Y. Liu, Y. Sun, X. Ma, X. Duan, C. Chen and Y. Wang, *J. Mater. Chem. A*, 2022, **10**, 24905-24914.
5. Y. Li, Z. Ding, X. Zhang, J. Li, X. Liu, T. Lu, Y. Yao and L. Pan, *J. Mater. Chem. A*, 2019, **7**, 25305-25313.
6. W. Kong, X. Ge, M. Yang, Q. Zhang, J. Lu, H. Wen, H. Wen, D. Kong, M. Zhang, X. Zhu and Y. Feng, *Desalination*, 2023, **553**, 116452.
7. D. Li, X. A. Ning, Y. Li and J. Zhang, *Environ. Sci. Nano*, 2020, **7**, 1980-1989.
8. Y. Li, Z. Ding, J. Li, J. Li, T. Lu and L. Pan, *Desalination*, 2019, **469**, 114098.
9. Z. Chen, X. Xu, K. Wang, D. Jiang, F. Meng, T. Lu, Y. Yamauchi and L. Pan, *Sep. Purif. Technol.* 2023, **315**, 123628.
10. L. Xu, Y. Liu, Z. Ding, X. Xu, X. Liu, Z. Gong, J. Li, T. Lu and L. Pan, *Small* 2024, **20**, 2307843.
11. A. Qian, H. Wu, G. Wang, N. Sun, H. Cheng, K. Zhang and F. Cheng, *ACS Appl. Mater. Interfaces*, 2023, **15**, 9203-9211.
12. Z. Chen, Z. Ding, Y. Chen, X. Xu, Y. Liu, T. Lu and L. Pan, *Chem. Eng. J.* 2023, **452**, 139451.
13. Z. Yang, P. Yang, X. Zhang, H. Yin, F. Yu and J. Ma, *Chem. Mat.*, 2023, **35**, 2069-2077.

14. K, Wang, L, Chen, G, Zhu, X, Xu, L, Wan, T. Lu and L. Pan, *Desalination*, 2022, **522**, 115420.
15. Y. Li, Y. Wang, Y. Cai, R. Fang and L. Zhang, *Desalination*, 2024, **577**, 117387.
16. J. Jin, M. Li, M. Tang, Y. Li, Y. Liu, H. Cao and F. Li, *ACS Sustain. Chem. Eng.*, 2020, **8**, 11424-11434.
17. G. Bharath, N. Arora, A. Hai, F. Banat, D. Savariraj, H. Taher and R. V. Mangalaraja, *Electrochim. Acta*, 2020, **337**, 135668.
18. G. Wang, T. Yan, J. Shen, J. Zhang and D. Zhang, *Environ. Sci. Technol.*, 2021, **55**, 11979-11986.
19. W. Si and H. Li, *Adv. Mater. Interfaces*, 2021, **8**, 2100125.
20. Z. Zhang and H. Li, *Environ. Sci. Nano*, 2021, **8**, 1886-1895.
21. Z. Liu and H. Li, *Energy Environ. Mater.*, 2023, **6**, e12255.
22. W. Xi and H. Li, *Environ. Sci. Nano*, 2020, **7**, 764-772.
23. Z. Li, H. Zhou and G. Wang, *J. Environ. Chem. Eng.*, 2024, **12**, 113277.
24. X. Wen, M. Zhao, Z. Zhao, X. Ma and M. Ye, *ACS Sustain. Chem. Eng.*, 2020, **8**, 7335-7342.
25. Z. Zhao, J. Zhao, Y. Sun, M. Ye and X. Wen, *Chem. Eng. J.*, 2022, **429**, 132582.
26. J. Du, W. Xing, J. Yu, J. Feng, L. Tang and W. Tang, *Water Res.*, 2023, **235**, 119831.
27. M. Gao, W. Liang, Z. Yang, T. Ao and W. Chen, *J. Colloid. Interface. Sci.*, 2023, **650**, 1244-1252.